nature communications

Article | Article in Press

https://doi.org/10.1038/s41467-026-78740-1

# Non-polar surface passivation of PbS Quantum Dots using metal thiolates enables photodiodes rivaling InGaAs performance

Received: 3 June 2026

Accepted: 1 October 2026

Published online: 22 October 2026

Check for updates

Debranjan Mandal[1], Yongjie Wang[1], Carmelita Rodá[1], Miguel Dosil[1], Gaurav Kumar[1], Lucheng Peng[1] & Gerasimos Konstantatos[1,2]

Colloidal quantum dots (CQDs) short-wave infrared (SWIR) detectors (1-2 μm) are of great interest for a plethora of applications including autonomous driving, machine vision, night and adverse weather imaging, in view of their low-cost and compatibility to read-out electronics. However, to date, CQDs photodetectors still suffer from high dark current and thereby noise such that their performance remains inferior to epitaxially grown III-V semiconductors. This performance gap originates from the limited passivation of non-polar surfaces existent in large PbS CQDs needed to access the SWIR spectral range. Here we report on a lead-thiolate based chemistry that serves to passivate both polar and non-polar surfaces of PbS CQDs yielding inks with unprecedented optoelectronic quality evidenced by open circuit voltage deficit and dark current activation energies matching those of single crystalline semiconductors. As a result, we demonstrate infrared photodetectors with remarkable thermal resilience, very low dark current density ( ~ 34 nA $cm^{-2}$ at −1 V) and a specific detectivity D* of ~$8\times10^{12}$ Jones. The measured D* value is on par with that of commercially available InGaAs photodiodes (PDs).

There has been an increasing demand for high-performance, cost-effective SWIR optoelectronic materials for applications such as autonomous driving[1], augmented reality[1,2], optical communications[3], bioimaging[4,5], surveillance[2,6], environmental monitoring, and food quality control[1,7]. Current SWIR optoelectronic materials primarily rely on epitaxially grown III-V semiconductors, yet, their high cost and limited compatibility with complementary metal-oxide-semiconductor (CMOS) integrated silicon circuits have hindered widespread adoption[2]. CQDs have emerged as a promising alternative due to their size-tunable bandgap, solution processability, and cost-effectiveness[1,7]. Lead chalcogenide CQDs, in particular, offer a large Bohr exciton radius, strong infrared absorption, and facile integration on various substrates[8]. The development of CQD-based IR optoelectronic devices has been driven by advancements in surface chemistry, enabling the assembly of CQDs into high-quality electrically conductive semiconductor thin films[9,10]. Traditionally, passivation strategies to concomitantly achieve low-trap state density and carrier transport in CQD films have relied on a layer-by-layer (LBL) solid-state ligand exchange method in which bulky oleate ligands are replaced by shorter molecules or even atomic ligands, facilitating surface passivation and charge transport[9]. The LBL approach, while versatile, comes with severe limitations in scalability, uniformity, and complete surface passivation[11]. To address these issues, the community has turned efforts towards the development of CQD inks, in which ligand exchange takes place in solution, enabling single-step deposition of optoelectronically active CQD thin films upon phase transfer to a polar solvent[11,12]. This leads to significant improvement in scalability, volume manufacturing, material consumption and yields thin films with lower defect- and trap-state densities and high-performance photodetectors[13–16], LEDs[17], and solar cells[11,12].

Despite progress, the resultant SWIR CQDPDs have failed, to date, to compete in performance with their epitaxial counterparts. While

[1]ICFO-Insitut de Ciencies Fotoniques, The Barcelona Institute of Science and Technology, Castelldefels, Barcelona, Spain. [2]ICREA-Institució Catalana de Recerca i Estudiats Avançats, Lluis Companys 23, Barcelona, Spain. e-mail: gerasimos.konstantatos@icfo.eu

CQD-based SWIR photodetectors are emerging as strong contenders in imaging and sensing applications, they still suffer from high dark current and noise levels compared to commercial InGaAs photodetectors[18,19]. We posit that the reason for this lies on the chosen chemistries to passivate the PbS CQD surface, relying on halide ions. Halide chemistry has been shown to be effective in passivating (111) facets of PbS CQDs, which is the dominant exposed surface plane in PbS CQDs that address the near infrared part of the spectrum[10,13]. Larger size CQDs with their bandgap extended in the SWIR progressively expose (100) non-polar surfaces on which halide chemistry has limited binding affinity[10]. We, therefore, took the view that in order to achieve stable and highly passivated PbS CQDs with bandgap tuned across the SWIR requires an alternative CQD ink chemistry. We posit that thiolate chemistry is more adequate to passivate larger PbS CQDs in view of the stronger binding affinity compared to halides. We therefore designed a ligand exchange process using lead acetate and 3-Chloro-1-propanethiol (CPT) for the ink formulation, in which the long ordered neutral metal thiolate moieties passivate the neutral nonpolar (100) facets. The solution phase exchanged QDs were found to exhibit compelling colloidal stability, CQD monodispersity and thermal stability in contrast to metal halide based CQD inks. Further, by employing this thiolate based ink technology, we report photodetectors with dark current density as low as 34 nA $cm^{-2}$ (1350 nm QDs) and 240 nA $cm^{-2}$ (1550 nm QDs), nearly two orders of magnitude lower than their halide counterparts and even 6 times lower than epitaxial raw InGaAs photodetectors at −1 V reverse bias. The detectors further demonstrate specific Detectivity ($D^*$) of $7.5 \times 10^{12}$ and $6.5 \times 10^{12}$ Jones at 1350 and 1550 nm, respectively, which is approximately an order of magnitude higher than prior reports of CQD PDs and comparable with commercially available InGaAs photodetectors.

## Results and discussion

### Lead thiolate PbS CQD Ink

Metal thiolates with lamellar structure have been employed as effective scaffolds for constructing nanosheets[20], QDs and metal nanoparticles[21], or used as effective passivants[22,23] for dispersion in polar solvents. Yet their demonstration as an optoelectronically active SWIR CQD ink has remained elusive. Here, in order to facilitate the ink formulation, we introduce a lead thiolate complex by mixing $Pb(Ac)_2{\cdot}3H_2O$ and CPT, as ligand precursor (Supplementary note 1), prior to solution phase ligand exchange of oleic acid (OA) capped PbS QDs. Figures 1a, b illustrate the schematics that describe the ligand exchange process of OA by the lead thiolate molecules on (100) and (111) facets, respectively. These layered precursors (Supplementary Fig. 1) can readily disassemble by mild heating or sonication, facilitating the exchange of long-chain OA molecules by the Pb-thiolate ligand. The resultant ink is named here as "thiolate ink" and metal halide ink as "halide ink". X-ray photoelectron spectroscopy (XPS) and FTIR analysis reveal that the surface chemistry of Pb-thiolate ink is distinct from CPT-only exchanged CQDs (see Supplementary Note 2 and 3 and Supplementary Figs. 2 and 3), confirming that the functioning unit is lead thiolate, instead of conventional thiol groups. XPS of Pb-thiolate inks on different-sized CQDs (see Supplementary Note 4 and Supplementary Fig. 4) also corroborates our hypothesis that neutral Pb-thiolate is an effective ligand on non-polar (100) facets via donor–acceptor coordination interactions involving both the sulfur and lead centers, consistent with the established L-/Z-type ligand framework for PbS nanocrystals, impeding the fusion of CQDs across those facets (Fig. 1a). For (111) facets, acetate binds as an X-type ligand and Pb-thiolate acts as an atomic ligand by replacing Pb-oleate through metathesis reaction as discussed in earlier reports[22] (Fig.1b). X-ray Diffraction (XRD) measurements (Supplementary Fig. 5) further support the findings by exhibiting the signature peaks of lamellar thiolate structure increasing with increasing size of dots. The Transmission Electron Microscopy (TEM) image of thiolate exchanged QDs exhibits distinctive (111) and (100) facets of QD (Fig. 1c).

Figure 1d compares the optical absorption and photoluminescence (PL) spectra of thiolate and halide PbS CQD inks. The thiolate ink maintains the size dispersity of the original OA-capped CQDs (Supplementary Fig. 6), exhibiting a peak-to-valley ratio of 8,

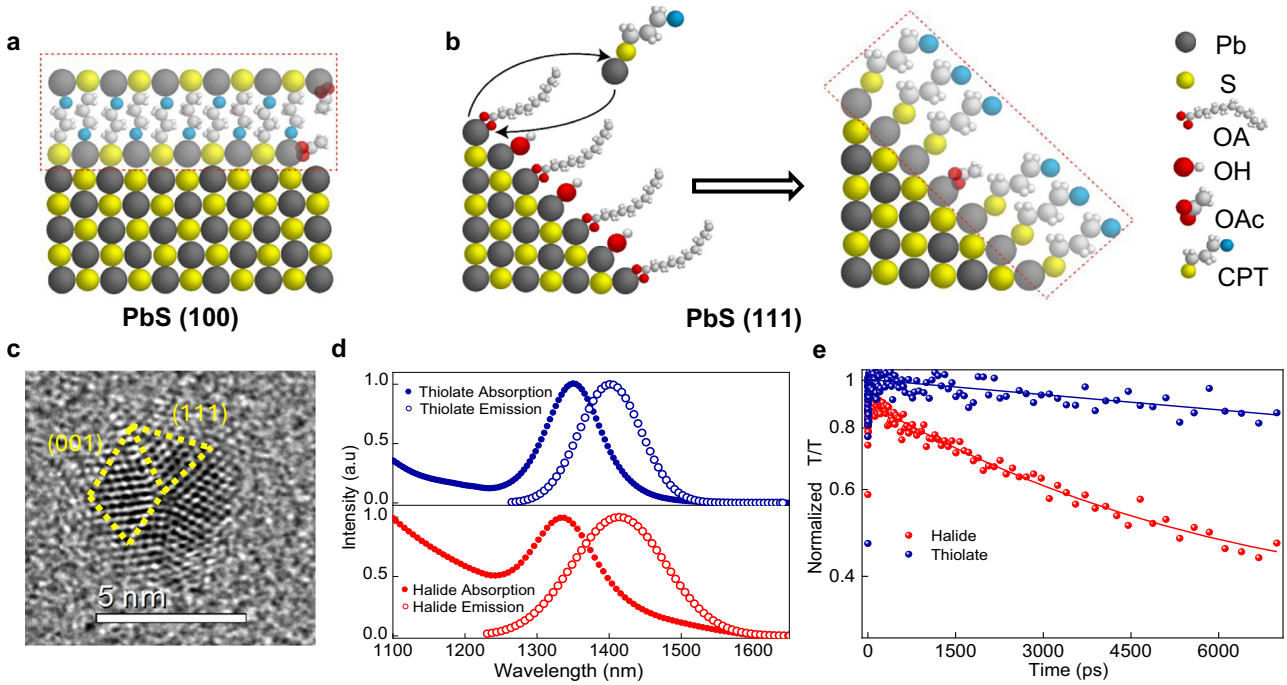


**Fig. 1 | Pb-thiolate exchanged PbS CQDs Ink. a** Schematic of PbS (100) surface passivation of thiolate-exchanged ink. **b** Schematic of PbS (111) surface passivation of thiolate ink. **c** TEM image of thiolate exchanged QD (scale bar represents 5 nm). **d** Solution phase absorption and photoluminescence (PL) spectroscopy of halide and thiolate exchanged QDs. **e** Normalized differential transmittance ($\Delta T/T$) of halide and thiolate ink films as a function of the pump-probe delay time. The samples were excited at 1160 nm with a pump fluence of 40 μJ/$cm^2$. Solid lines are fits to the decays of the thiolate and halide films.

https://doi.org/10.1038/s41467-026-78740-1

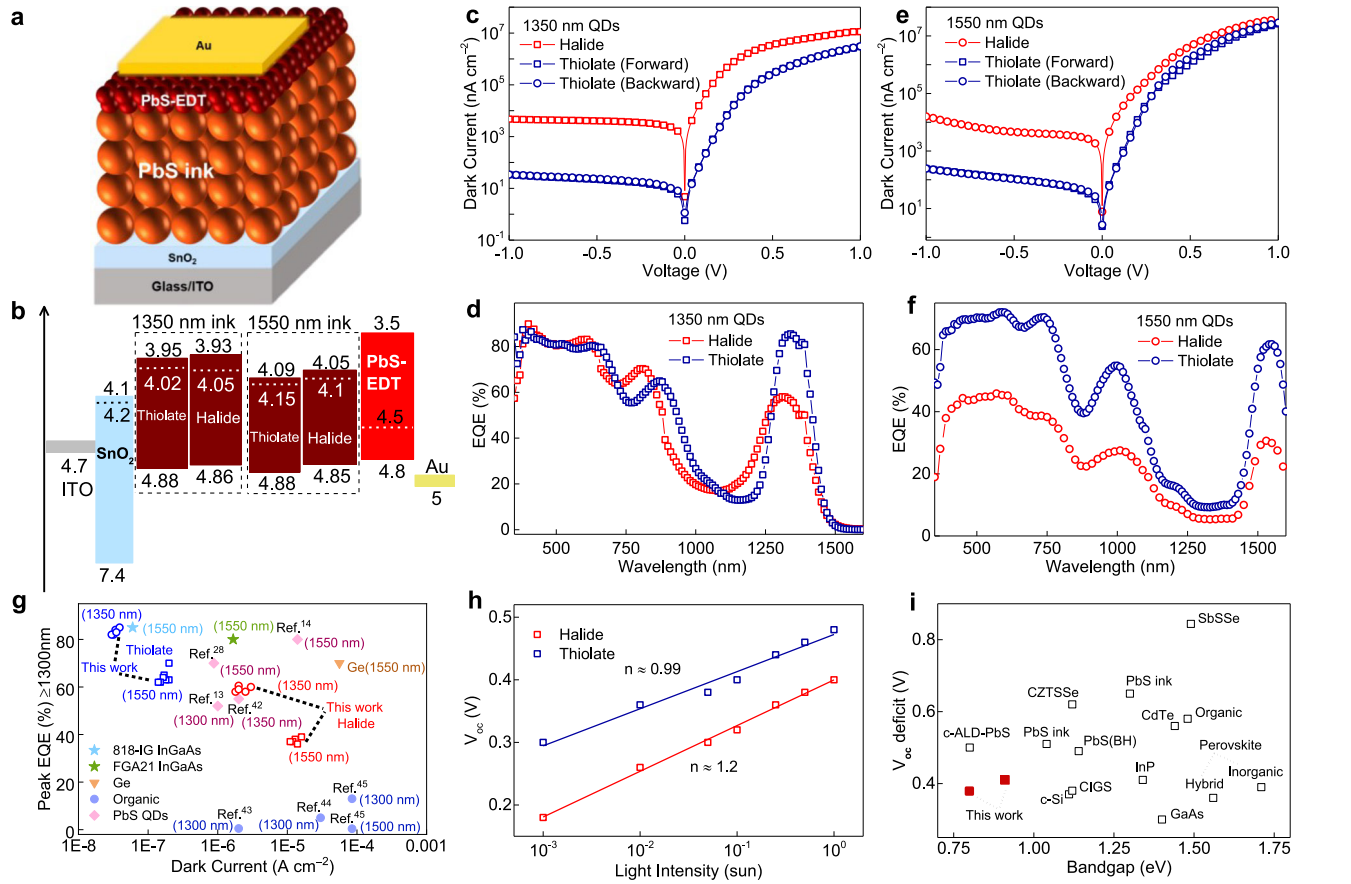


**Fig. 2 | PbS CQD SWIR PD. a** Schematic of PbS CQDs PDs. **b** Band diagram of thiolate and halide PbS CQDs ink PD device for 1350 nm and 1550 nm QDs based on UPS measurements. **c** Dark current density-voltage (J-V) curves of 1350 nm Qs PD devices. **d** EQE spectrum of 1350 nm halide and thiolate QDs ink PDs, at 0 V bias. **e** J-V curves of 1550 nm QDs PD devices. **f** EQE spectrum of 1550 nm halide and thiolate QDs ink PDs, at 0 V bias. **g** Plot of the maximum EQE for wavelengths ≥1300 nm versus dark current density at −1 V reverse bias for PbS QDs[13,14,28,42], Organic[43–45], InGaAs (Raw PD Thorlabs-FGA21, electronically mounted and calibrated Newport 818-IG) and Ge (Thorlabs-FDG03). The EQE at 0 V bias is plotted. **h** Light Intensity dependent $V_{oc}$ of halide and thiolate PDs. **i** $V_{oc}$ deficit of thiolate ink based diode comparison with reported solar cells under AM1.5 G solar simulator[11,28,31,46].

while conventional halide ink results in a broad size distribution (with a peak-to-valley ratio of 1.64) due to fusion of dots[24]. This is in accordance with TEM data shown in Supplementary Fig. 7 and the PL full width half maxima (FWHM) (Supplementary Table 1). The colloidal stability of the PbS QDs in polar solvents has been a well-known obstacle for halide-based methods[10]. While halide exchanged CQDs exhibit rapid precipitation within approximately 30 min after ligand exchange, thiolate exchanged CQDs maintain long-term colloidal stability, with no significant changes in the absorption peak position or FWHM during systematic monitoring over one week and even no observable precipitation after at least one month of storage (Supplementary Fig. 8). Last, we sought to assess the degree of passivation of the thiolate ink, therefore we measured the photoluminescence quantum yield (PLQY) of the thiolate ink in solid state thin film which found out to be ~3%, whereas the halide ink's PLQY is < 0.1% (see Supplementary Note 5 and Supplementary Fig. 9). We also measured the excited state carrier dynamics of solid-state films from halide and thiolate inks (Fig. 1e). The carrier lifetime on the halide ink is measured to be ~4 ns (3.98 ± 0.5 ns) whereas the carrier lifetime of the thiolate ink is estimated to be ~40 ns. The realization of long carrier lifetimes underpins the performance of minority carrier-driven optoelectronic devices such as PDs and solar cells, for it determines both the quantum efficiency and the reverse dark current, thereby the detectivity in a PD and the open circuit voltage in a solar cell. Long carrier lifetime ($\tau$) benefits quantum efficiency as the carrier diffusion length ($L$) scales as, $L = \sqrt{D\tau}$ where $D$ is the diffusion coefficient proportional to carrier mobility. Moreover, long carrier lifetime is beneficial for reduced dark current: First, the reverse saturation current that is generated by minority carrier diffusion across the junction scales inversely proportional to the square root of carrier lifetime. Second, and most relevant for the devices considered herein – characterized by the presence of surface states (trap states) of CQDs – the generation-recombination (G-R) current in the depletion region scales inversely proportional to the carrier lifetime.

## PbS CQDs SWIR PDs based on the thiolate ink

To evaluate the impact of the highly passivated thiolate ink on the performance of CQD photodetectors, we fabricated PDs based on the halide ink and thiolate ink for two sizes of dots with exciton peaks at 1350 nm and 1550 nm. The device structure comprised the following layers: ITO/$SnO_2$/PbS QDs ink/PbS-EDT (1,2 -Ethanedithiol)/Au (Fig. 2a), and the corresponding band levels are shown in Fig. 2b (see Supplementary Note 6 and Supplementary Figs. 10, 11). A cross-sectional SEM image of the device is shown in Supplementary Fig. 12. To understand the operating principle of thiolate-ink-based devices, control devices, each comprising a single heterojunction, confirm that the primary junction forms at the $SnO_2$/thiolate ink interface, consistent with an n-type QD/Electron transport layer (ETL) heterojunction while the Hole transport layer (HTL), PbS-EDT mainly improves back-contact passivation thanks to its electron blocking character (See Supplementary Note 7 and Supplementary Fig. 13). The n-type doping of thiolate ink is

further validated by Mott–Schottky capacitance–voltage analysis (Supplementary Note 8 and Supplementary Fig. 14).

The thiolate ink-based diodes exhibit a dark current density two orders of magnitude lower than their halide ink counterparts (Fig. 2c, e) with the thiolate ink-based diodes for 1350 nm and 1550 nm CQDs showing dark current densities at −1 V as low as 34 nA cm$^{-2}$ and 240 nA cm$^{-2}$, respectively. Further, diode analysis[13,25] (see Supplementary Note 9 and Supplementary Fig. 15) shows that the reverse saturation current density $J_0$ for the thiolate device, is lower than their halide ink counterparts. Moreover, the thiolate ink diodes do not show any signs of non-ohmic leakage current, indicative of the absence of interface defects and trap-assisted tunneling current under bias[13]. The higher shunt resistance of thiolate ink devices (2.88 MΩ·cm$^2$) compared to the halide-based ones (28.5 kΩ·cm$^2$) leads to a reduction in the ohmic leakage current density (85 nA cm$^{-2}$ for the halide-based diode and 13 nA cm$^{-2}$ for the thiolate-base diode). Further, we measured the external quantum efficiency (EQE) for both classes of devices as shown in Fig. 2d, f. Optical simulations using Transfer Matrix Method (TMM) (see Supplementary Note 10 and Supplementary Figs. 16,17 and 18) are in agreement between stimulated and experimental EQE for both halide and thiolate 1350 nm QDs device, the higher SWIR EQE of thiolate devices arises from more efficient carrier extraction, whereas halide devices, particularly with 1550 nm QDs, suffer from inefficient electron and hole extraction. Since carrier mobilities are comparable for both halide- and thiolate-based QDs (see Supplementary Note 11 and Supplementary Fig. 19 and 20), the markedly longer minority carrier lifetime in thiolate devices becomes the determining factor, extending the diffusion length and thereby enhancing EQE with supressed dark current. Figure 2g summarizes the key figures of merit discussed above for the two ink technologies along with reported CQD and commercial bare and calibrated InGaAs PDs (Supplementary Fig. 21). Statistical analysis (see Supplementary Note 12 and Supplementary Figs. 22, 23) confirms that thiolate-based CQD devices achieve consistently enhanced performance compared to their halide-based counterparts.

Such drastic improvements in the diode quality of the thiolate inks compared to halide ones is underscored by a nearly one order of magnitude reduction in trap state density based on photo-induced current transient spectroscopy[26] (see Supplementary Note 13 and Supplementary Fig. 24). The activation energy ($E_a$) from temperature-dependent dark current analysis provides further valuable insight into recombination processes in PDs. In our heterojunction ($n^+$–n – p) device architecture, recombination is likely determined by interface recombination[27] (see Supplementary Note 14 and Supplementary Figs. 25, 26). For thiolate-treated devices, the extracted $E_a$ closely matches the Fermi-level offset between the active layer and the PbS-EDT electron-blocking layer, whereas the lower $E_a$ in halide-treated devices suggests interface recombination from electron trap-states in the halide-based active layer and holes of the PbS HTL. The quality of the thiolate ink diodes also motivated us to test them as photovoltaic solar cell devices (see Supplementary Note 15). As expected, the thiolate-based solar cells outperform the halide ones by delivering power conversion efficiency of 9.7% and 6% for 1350 nm and 1550 nm QDs (Supplementary Figs. 27, 28), the highest reported to date for SWIR CQD solar cells[10,28,29]. To further elucidate the recombination pathways in our solar cells, we measured the intensity dependence of the open-circuit voltage ($V_{oc}$). For thiolate-treated solar cells, the ideality factor is near unity ($n \approx 1$), indicating a band-to-band recombination process at $V_{oc}$ condition (Fig. 2h). In contrast, halide-treated devices exhibit $n \approx 1.2$, suggesting contributions from trap assisted recombination at surfaces or interfaces[30]. As a result, solar cells based on thiolate exchanged QDs reached record high $V_{oc}$ of ~ 0.5 V, leading to a $V_{oc}$ deficit of 0.4 V, on par with that of perovskite, Si and copper indium gallium selenide (CIGS) solar cells[31]. Since the maximum achievable $V_{oc}$ is fundamentally determined by the emission energy rather than the absorption onset[32], the reduced Stokes shift of thiolate inks arising from their higher monodispersity[33], suppression of band-tail states[11], and reduced defect states[34] leads towards band-edge dominated recombination and consequently a lower $V_{oc}$ deficit.

Next, we wanted to assess the sensitivity and key photodetector characteristics of thiolate CQD inks. For practical integration of PDs on image sensor read-out electronics, it is the low-frequency noise that determines the specific detectivity, which in turn governs the imager's ability to operate under low-signal conditions, thus the performance of the detector at low frequency is very much crucial for any practical implementation on image sensor applications. By measuring the noise current of our devices (see Supplementary Note 16 and Supplementary Figs. 29–32), we plot in Fig. 3a the spectral D$^*$ of the photodetectors under study. The high dark current of halide inks leads to a drastic increase in noise for this class of detectors, limiting their peak detectivity to $9 \times 10^{11}$ Jones for 1350 nm PbS CQDs and $1.5 \times 10^{10}$ Jones for the 1550 nm PbS CQDs. On the other hand, the thiolate-based devices exhibited very low noise current (Supplementary Figs. 31, 32), resulting in peak D$^*$ of $7.5 \times 10^{12}$ Jones for 1350 nm and $6.5 \times 10^{12}$ Jones for 1550 nm PbS CQDs. The measured noise spectral density is predominantly limited by the Johnson noise of PDs and remains constant across the measured frequency range whereas the 1550 nm halide ink device exhibits a clear 1/f noise ($\gamma \approx 0.85$ which represents the power law exponent for the frequency dependance) upto 100 Hz, indicative of trap-assisted carrier fluctuations, followed by a transition to Johnson noise at higher frequencies This indicates that the report of D*, in this class of devices, at high frequencies does not guarantee similar performance at lower frequencies that are relevant for imaging applications. Figure 3b summarizes the frequency-dependent D$^*$ of our detectors with prior reports of CQD SWIR PDs as well as commercially available state-of-the-art epitaxial InGaAs detectors. Based on the measured noise current densities of several representative devices, the corresponding specific detectivity (1 Hz) distributions at the peak wavelengths are plotted in Supplementary Fig. 33.

The measured D$^*$ of the thiolate ink-based photodetector in this report, to the best of our knowledge, still outperforms all reported CQD-based photodetectors even though those were reported at a higher frequency range. Details of the literature review on dark current, EQE and D$^*$ of PbS QDs IR detectors is presented in Supplementary Table 4.

As the noise of our detector is found to be independent of frequency and governed by the Johnson noise limit we found that our thiolate ink device (1550 nm QDs) exhibits similar level of noise power density with high sensitivity grade commercial Newport 818-IG InGaAs and lower than the Thorlabs InGaAs FGA21) detector resulting to comparable values of D$^*$ at 1350 nm and 1550 nm with 818-IG and higher than the raw InGaAs (FGA21) (Fig. 3c). To our knowledge, this is the first record of any CQDs PDs to match the performance of a single crystalline semiconductor technology counterpart.

We also measured the linear dynamic range (LDR) of the detectors with thiolate-based devices, yielding an LDR of 172 dB (Fig. 3d). The LDR of the halide ink is measured as ~ 130 dB. As shown in Fig. 3b, the minimum detectable intensity from the thiolate ink is as low as 10 pW·cm$^{-2}$, which in turn yields a specific detectivity of $2 \times 10^{12}$ Jones, in agreement with the value extracted from the noise measurements. Last, we characterized the time response of our detectors. From frequency dependent response, we calculated the − 3 dB bandwidth of the thiolate device to be about 151 kHz for 1350 nm and 232 kHz for 1550 nm QDs (Supplementary Fig. 34). Response times were further evaluated from transient photocurrent measurements[14] (see Supplementary note 17 and Supplementary Fig. 35) across different pixel areas. Thiolate devices consistently exhibit faster responses than halide devices (180 ns vs. 410 ns for a 0.04 mm$^2$ pixel), and bias-dependent measurements show that both device types achieve sub-100 ns response times at 1 V bias for a 0.09 mm$^2$ pixel. By further

https://doi.org/10.1038/s41467-026-78740-1

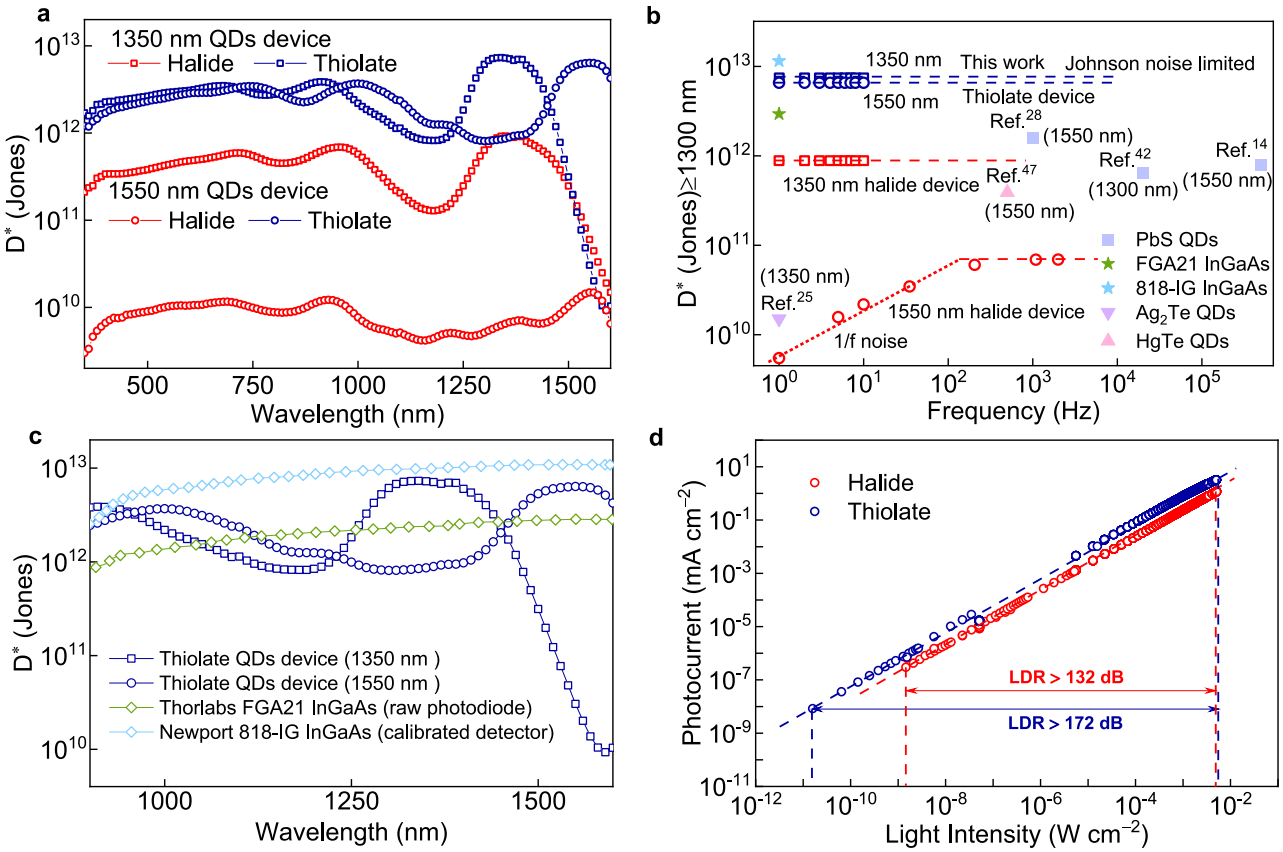


**Fig. 3 | Characteristics of PbS CQDs PD. a** Specific detectivity spectrum of thiolate and halide ink for 1350 nm and 1550 nm QDs at 100 Hz, at 0 V bias. **b** Frequency dependent detectitvity of SWIR PDs ≥ 1300 nm with literature (PbS[13,14,28,42], $Ag_2Te$[25], and HgTe[47] QDs). The dashed line indicates Johnson noise limited detectivity, and the dotted line identifies 1/f noise limited detectivity. **c** Wavelength-dependent detectivity of SWIR QDs PDs with commercial Thorlabs raw PD InGaAs (FGA21) and electronically calibrated Newport 818- IG InGaAs detector. **d** LDR of PbS QDs ink PD under 1350 nm pulse light illumination with power densities 0.01 nW/cm² to 8 mW/cm².

increasing the bias to 2 V the thiolate-based PbS QD devices can reach response times as low as 25 ns (Supplementary Fig. 36). Such response times are sufficiently short for most imaging applications (video-frame and machine vision).

## Material and device thermal stability

When it comes for a technology to enter the market, besides compelling performance, thermal stability is also a prerequisite to enable robust product manufacturing. We posited that thiolate chemistry would offer substantially improved material thermal stability and subsequently device thermal resilience over halide chemistry, in view of the stronger binding energies of thiolates over halide to Pb cations. We therefore performed a thermal stability analysis of our thiolate-based PbS CQD inks and compared with their halide counterparts. We hypothesized that the weak ligand binding of halides on (100) facets of PbS CQDs allows for CQD fusion along this axis[35,36] upon thermal stress (Fig. 4a), whereas thiolate ligands would prevent fusion upon annealing (Fig. 4b). TEM images of both halide and thiolate based CQD inks confirmed this hypothesis, as shown in Fig. 4c–f. Halide-exchanged CQD inks were found to fuse after 1 hour of annealing at 100 °C (Fig. 4c, d), it was difficult to obtain a reliable particle size distribution, while thiolate ink exhibits a minimal change in average particle size (Supplementary Fig. 37).

To probe further the structural changes upon annealing, we recorded the XRD patterns for different temperature-annealed films. With increasing temperature, changes in the XRD peak widths were observed, indicating an increase in the crystallite size (Fig. 4g, h). We calculate the average crystallite size from peak width analysis (see Supplementary Note 18); It is found that the thiolate-based ink maintains a crystal size of ~ 4 nm up to 130 °C whereas the halide-based ink exhibits an increase in crystallite size to 5.3 nm for the same conditions. As shown in Fig. 4g, crystal grain growth sharply onsets at 130 °C for the halide-based inks. At 160 °C, additional small and narrow peaks are observed for halide ink, which is indexed to $PbBr_2$, following the prior report for chlorine passivated PbS QDs[37]. Further probing annealing time at 100 °C, the halide ink shows a gradual broadening of peak widths, whereas the thiolate ink preserves nearly constant widths even up to 14 h (Fig. 4i, j).

XRD analysis also suggests that thermal degradation of CQD solids involves ligand desorption, facet reconstruction, and interparticle fusion. In thiolate-passivated CQDs, the observed crystallite growth along the (200) direction may be related to the presence of Pb-S surface motifs that promote fusion between neighboring CQDs upon annealing. In halide-passivated CQDs, preferential stabilization of the (111) facets leads to enhanced growth along the (200) direction after ligand exchange (Supplementary Fig. 38), while subsequent ligand loss facilitates CQD coalescence and further crystallite growth. However, the detailed degradation pathway remains unclear and will require more in situ temperature-dependent structural characterizations techniques to directly probe ligand desorption, facet evolution, and CQD fusion during annealing.

CQD fusion in turn affects their optical properties, causing an increase of the FWHM of the exciton peak absorption spectra with temperature. The FWHM of halide ink increases from 134 nm (room temperature) to 151 nm at 100 °C, while no exciton peak can be observed upon further increasing the temperature to 130 °C

https://doi.org/10.1038/s41467-026-78740-1

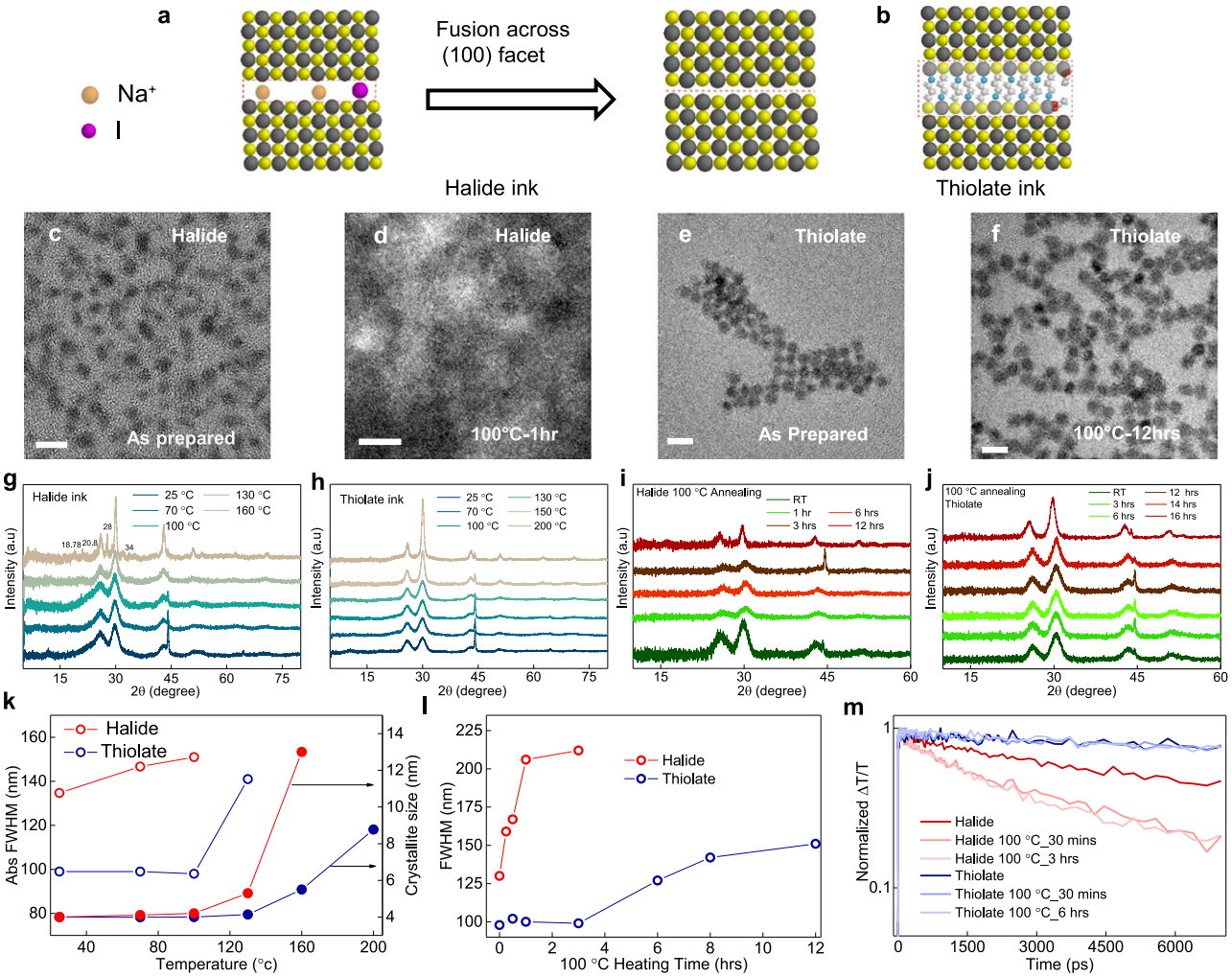


**Fig. 4 | Stability of QD inks. a** Schematic of halide ink fusion across (100) facet. **b** Schematic of restriction of fusion of thiolate ink across (100) facet. **c** TEM image of as prepared halide ink and (**d**) after annealing 100 °C for 1 hr, TEM grids are annealed after drop casting ink (0.1 a.u). For thiolate ink TEM image of (**e**) As prepared (**f**) 100 °C annealed for 12 hrs. Scale bar of Fig. 4c–f represents 10 nm. XRD patterns of (**g**) halide ink (**h**) thiolate ink films annealed at different temperature and (**i**), halide ink (**j**), thiolate ink films annealed at 100 °C for varying annealing times. **k** Change of absorption FWHM and crystallite size of both halide and thiolate ink films with different annealed temperature for 30 min from thin film absorption and XRD measurements. **l** Change of absorption FWHM for different annealing time at 100 °C from thin film absorption spectra. **m** Normalized differential transmittance ($\Delta T/T$) of halide and thiolate ink films as prepared, after annealing for 30 min and 6 h (3 hours) at 100 °C as a function of the pump-probe delay time. The samples were excited at 1160 nm with a pump fluence of 40 μJ/cm$^2$.

(Supplementary Fig. 39). On the other hand, the thiolate exciton peak maintains a constant FWHM of 100 nm up to 100 °C increasing to 140 nm at 130 °C (Fig. 4k). Under constant-temperature annealing at 100 °C, the halide peak vanishes after 4 h, but the thiolate peak persists even after 12 h (Supplementary Fig. 40). The FWHM of halide inks broadens continuously, whereas the thiolate-based one shows negligible change up to 3 h and only a 35 nm increase after 12 h (Fig. 4l).

To further characterize the chemical alterations on the QD surface, we performed XPS analysis. From XPS analysis, we recorded a reduction in the S/Pb ratio of halide ink with annealing, while the S/Pb ratio for thiolate ink remains almost constant throughout annealing. The initial S reduction is likely due to the removal of the excess Pb-thiolate or CPT ligands (Supplementary Fig. 41). Halide inks exhibit a pronounced increase in the Pb-oxidation peak (529.8 eV) upon annealing, whereas thiolate inks show no increase in Pb–O peak intensity upon annealing, indicating effective protection against surface oxidation and improved passivation compared to halide inks. We also performed thermogravimetric mass spectrum analysis to monitor the mass loss upon temperature; the thiolate ink lost 1.5% of its initial mass, whereas the halide ink lost 3.1%, both at 200 °C (Supplementary Fig. 42). The onset of mass loss for halide ink was found to be at ~ 40 °C, whereas the mass loss onset of the thiolate ink was at 120 °C. The intensity of detectable mass loss for halide ink is much higher than thiolate ink (Supplementary Fig. 43).

To further elucidate on the effect of temperature on the optoelectronic properties of the materials related to device performance, we first performed transient absorption spectroscopy (TAS) to probe the carrier lifetime. Halide-based CQD inks were found to exhibit broadening of their transient absorption spectrum upon increasing annealing time at 100 °C whereas thiolate-based inks preserved their spectrum in agreement with linear absorption measurements (Supplementary Fig. 44). Kinetics were found to be affected accordingly with halide-based ink showing acceleration of the carrier lifetime to ~ 2 ns, whereas thiolate ink maintains the initial carrier lifetime even after 6 h of annealing at 100 °C (Fig. 4m).

Another critical measure of the quality of an optoelectronic material is its photoluminescence (PL). Thiolate ink films of 1350 nm PbS QDs retain PL up to 130 °C, whereas halide films lose PL after 50 °C (Supplementary Fig. 45). Notably, 1550 nm thiolate QDs show even narrower absorbance and PL FWHM up to 130 °C, consistent with

https://doi.org/10.1038/s41467-026-78740-1

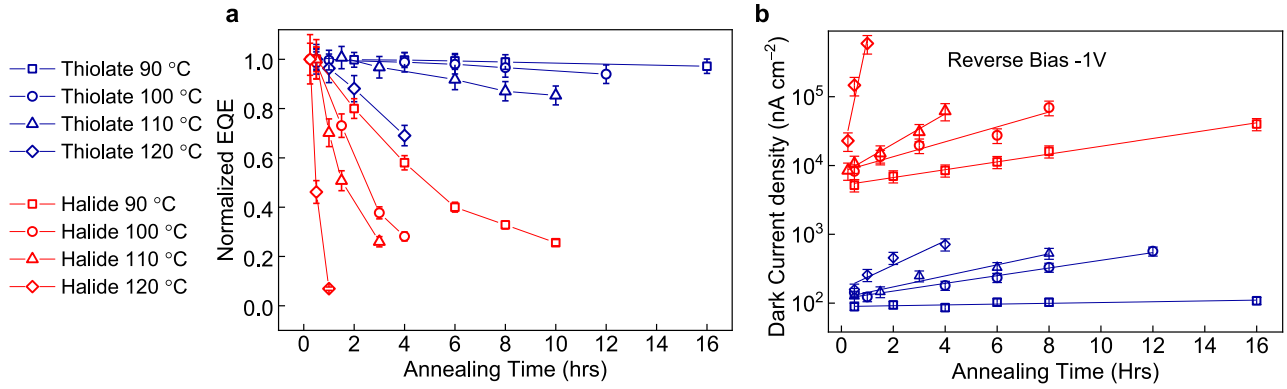


**Fig. 5 | Stability of PbS CQDs PDs. a** Normalized EQE with standard deviation error bar of halide and thiolate ink PDs at zero bias upon different annealing temperatures for different periods of time. **b** Dark current density with standard deviation error bar of photodiodes at − V reverse bias for different time intervals at different annealing temperatures.

thermal stability observed in absorption FWHM after 8 h at 100 °C (Supplementary Figs. 46–48). This supports our hypothesis that Pb-thiolates are more effective in stabilizing the QDs at (100) facets as larger sized QDs feature larger (100) facets[38] (Supplementary Fig. 47). In contrast, halide 1550 nm QDs exhibit weak PL even at room temperature due to poor passivation (Supplementary Fig. 46). Our study indicates that halide chemistry is not adequate to passivate and stabilize PbS QDs for the SWIR.

Having studied the material thermal stability, we, next, sought to investigate the thermal stability of PDs. After stack fabrication, we performed annealing as described in the methods section, followed by contact metallization. Then, we measured the dark J-V and EQE of all the devices at different time intervals for each annealing temperature (Supplementary Figs. 49–52). Figures 5a, b plot the normalized peak EQE value and the dark current at − 1 V reverse bias of the devices as a function of annealing time at various temperatures. The results show a significant improvement in device thermal stability for thiolate inks over the halide inks. The emergence of $PbX_2$ diffraction peaks (Fig. 4g) for halide ink after thermal aging suggests a similar degradation mechanism of lead-halide chemistry [39–41] in view of the halide-inks being akin to lead-halide perovskites, particularly halide migration and decomposition into the thermodynamically favorable $PbX_2$ containing phase.

In summary, this work has shown that the traditionally used halide chemistry for SWIR PbS CQD optoelectronics is not adequate to enable highly passivated and robust SWIR CQDs for optoelectronic devices with competitive performance. We further demonstrate that PbS CQD inks based on lead thiolate ligands yield high optoelectronic grade quality CQD thin films along with drastically improved thermal stability compared to their halide counterparts. PDs based on thiolate ink CQDs demonstrate compelling performance in the SWIR region with dark current two orders of magnitude lower and an-order-of-magnitude higher specific detectivity than prior state-of-the-art SWIR CQD PDs. The enhanced detectivity of thiolate-based devices arises from a synergistic combination of improved passivation and long carrier lifetime, which together enhance charge extraction, suppress trap-assisted recombination, reduce dark current and thereby noise. A key advantage of this thiolate CQDs ink technology is its compatibility with monolithic integration on silicon CMOS readout circuits through solution-processable deposition methods. In contrast to conventional InGaAs image sensors, which rely on costly III–V semiconductor growth and indium bump-bond hybridization, the presented approach offers a scalable and potentially lower-cost pathway toward high-resolution SWIR image sensors. These results, therefore, represent an important step toward commercially viable infrared imaging technologies that combine InGaAs-level performance with CMOS-compatible manufacturing.

## Methods

### Synthesis of PbS QDs

PbS QDs with an excitonic peak ~1320 nm are synthesized by a previously reported multi-injection method [30]. Typically, 446 mg PbO, 3.8 mL oleic acid and 50 mL octadecene (ODE) were kept under vacuum for 2 hours at 95 °C. Once the transparent, clear solution of lead oleate is formed, the reaction condition is transformed from vacuum to Argon and the reaction temperature is raised to 100 °C. A solution of 90 μL hexamethyldisilathiane (TMS) in 3 mL ODE is quickly injected, then after 6 min, a second injection of 65 μL of TMS in 9 mL ODE is added dropwise. Then the heating is stopped immediately, and the solution is cooled down gradually to room temperature. After reaching at room temperature, the QDs are precipitated by adding acetone, followed by centrifugation. The QDs are further purified for another three times by dispersing and precipitating using toluene/acetone as solvent/antisolvent. The final QDs are dispersed in octane with a concentration of 30 mg/mL for solution-phase ligand exchange. For 1520 nm QDs, A solution of 70 μL hexamethyldisilathiane (TMS) in 3 mL ODE is quickly injected, then after 6 min, a second injection of 100 μL of TMS in 9 mL ODE is added dropwise. Purification steps are followed similar as 1320 nm QDs.

### Solution phase ligand exchange

Halide ink is prepared as mentioned in the previous reports[10,14]. For thiolate ink, the lead thiolate complex is first made by adding an equal ratio of lead acetate (0.1 M) and thiol ligand (0.1 M) in polar DMF solvent. The mixture is vortexed for some minutes to get a clear solution of lead thiolate complex. The oleic acid capped QDs solution is diluted to 10 mg/mL in octane. A 5 ml amount of CQD octane solution to 5 mL lead thiolate ligand precursor solution. Both the solution is mixed vigorously until a clear phase separation is observed. The top octane phase is discarded, and further 5 mL octane is added and discarded again after mixing vigorously. This step is repeated for another two times. QDs in DMF are precipitated via the addition of methanol. After centrifugation, the QDs are dried under vacuum for 30 min. Dried CQDs powder are dispersed in the mixture of butylamine: DMF (4:1) solvent, depending on the desired concentration of ink.

### Characterization of QDs ink

A Cary 5000 UV-Vis-NIR spectroscope were used for Ultraviolet–visible-IR absorption measurements for solution and thin films. Stead state PL measurements were performed using a Horiba Jobin Yvon iHR550 Fluorolog system coupled with a Hamamatsu

RS5509-73 liquid-nitrogen cooled photomultiplier tube and a calibrated Spectral on-coated Quanta-phi integrating sphere. For PLQY measurements, a four-channel Thorlabs laser was used as the excitation light and a Kymera 328i spectrograph (Oxford Instruments, Andor) was used as the detector ( < 1600 nm). The X-ray diffraction data were collected using a Rigaku SmartLab powder diffractometer in the Bragg–Brentano geometry with Cu Kα radiation on drop-cast powder samples. Complex refractive indices, ($\check{n} = n + ik$), were extracted from the CQD films using an RC2 variable angle spectroscopic ellipsometer (Woolham). Transient absorption spectroscopy was carried out using an automated femtosecond transient absorption spectrometer (Helios, Ultrafast System). TEM was performed at the Scientific and Technological Centers of the University of Barcelona. The TEM images were obtained using a JEOL 2100 microscope operating at an accelerating voltage of 200 kV. The TEM samples were prepared by dropping a diluted QD solution on ultrathin carbon grids. The X-ray photoelectron spectroscopy/ultraviolet photoelectron spectroscopy measurements were performed with a SPECS PHOIBOS 150 hemispherical analyzer under ultrahigh-vacuum conditions ($10^{-10}$ mbar) at the Institut Català de Nanociència i Nanotecnologia. The thermogravimetric mass analysis is carried out by a NETZSCH TG-EGA system equipped with TGA/STA 449 F5 Jupiter thermobalance.

### Device fabrication

All the device fabrication steps were carried out in ambient air. ITO-covered glass substrates (Universität Stuttgart, Institut für Großflächige Mikroelektronik) were cleaned by sonication in soap water, acetone and isopropanol for 20 min each and dried with nitrogen, followed by 0.5 h of ultraviolet/ozone treatment. A $SnO_2$ electron transport layer was then deposited with an atomic layer deposition technique at 150 °C to achieve a thickness of ~ 20 nm. The active layer of PbS QDs ink was spin coated on $SnO_2$ substrate with 2500 rpm. Then, two PbS-EDT layers were fabricated via a layer-by-layer method. Oleic-acid-capped CQDs were deposited, and then a 0.01 vol% EDT in acetonitrile solution was applied to the film for 30 s, followed by a 3-time acetonitrile rinsing step. Finally, a Kurt J. Lesker NANO 36 system was used to deposit 100 nm Au as the top electrode with a device area of 3.14 $mm^2$. The device area is fixed at 3.14 $mm^2$ for all measurements. Only response time studies were performed on devices with varying areas, from 3.14 $mm^2$ to 0.04 $mm^2$. For thermal degradation study of PDs, we anneal the QDs layers at various temperatures for different period prior to Au deposition as the metal electrode (Au) can easily diffuse in QDs stack during the high temperature annealing and which can enhance the dark current and reduce the photocurrent of the device.

### Device characterization

All the device characterizations were performed in air under ambient conditions. Current–voltage ($J$–$V$) measurements were performed with a Keysight semiconductor parameter analyzer (B1500A) with the devices kept in a shield box. The EQE value was measured using a Newport Cornerstone 260 monochromator, a Thorlabs MC2000 chopper, a Stanford Research SR570 transimpedance amplifier and a Stanford Research SR830 lock-in amplifier. Calibrated Newport 818-UV and 818-IR photodetectors were used as the reference. The TOF was measured using a nanosecond laser with a wavelength of 520 nm. Photocurrent decay was recorded with varying biases using an oscilloscope. Noise current was measured from an MFLI 500 kHz lock-in amplifier using its noise amplitude sweep method combined with a DLPCA-200 low noise current amplifier. All measurements were performed in a shielded and electrically grounded enclosure at dark, room temperature conditions. The noise floor and bandwidth are first cross-checked at a variable gain of the preamplifier. Then further, we measured the noise of 100 MΩ, 1.0275 MΩ and 100 kΩ resistor to validate the setup, which are exactly matched with their Johnson noise level (see Supplementary Note 16). For all the device measurements we set the preamplifier sensitivity 1 nA $V^{-1}$ (unless it is mentioned otherwise). To measure the 3 dB bandwidth, a nanosecond laser (520 nm) was used as incident light, which was modulated by a waveform generator (Agilent 33220 A) at various frequencies with a 50% duty cycle. The output current was recorded with an oscilloscope. The response time was extracted from the 10–90% interval of the transient photocurrent under 650 nm nanosecond laser excitation (20 ns pulse width, 1 kHz repetition rate). For LDR measurements, a four-channel laser (Thorlabs) at 1350 nm was used as the light source at a frequency of 7 Hz modulated by an Agilent waveform generator. The light was directed by a beam splitter to a Newport 818-IG detector and the device. The current was amplified by SR570 amplifiers and recorded by an oscilloscope.

## Data availability

All data that support the findings of this study are presented in the manuscript and the Supplementary information. Source data are provided in this paper.

## References


1. García de Arquer, F. P. et al. Semiconductor quantum dots: Technological progress and future challenges. *Science* **373**, https://doi.org/10.1126/science.aaz8541 (2021).
2. Horiuchi, N. Infrared applications. *Nat. Photon.* **13**, 376–377 (2019).
3. Dholakia, K. & Bruce, G. D. Optical hooks. *Nat. Photon.* **13**, 229–230 (2019).
4. Naczynski, D. J. et al. Rare-earth-doped biological composites as in vivo shortwave infrared reporters. *Nat. Commun.* **4**, 2199 (2013).
5. Zhang, T. et al. Six-arm stellat dendritic-PbS flexible infrared photodetector for intelligent healthcare monitoring. *Adv. Mater. Technol.* **7**, 2200250 (2022).
6. Tang, X., Ackerman, M. M., Chen, M. & Guyot-Sionnest, P. Dual-band infrared imaging using stacked colloidal quantum dot photodiodes. *Nat. Photon.* **13**, 277–282 (2019).
7. Almutlaq, J. et al. Engineering colloidal semiconductor nanocrystals for quantum information processing. *Nat. Nanotechnol.* **19**, 1091–1100 (2024).
8. Saran, R. & Curry, R. J. Lead sulphide nanocrystal photodetector technologies. *Nat. Photon.* **10**, 81–92 (2016).
9. Ip, A. H. et al. Hybrid passivated colloidal quantum dot solids. *Nat. Nanotechnol.* **7**, 577–582 (2012).
10. Kim, Y. et al. A facet-specific quantum dot passivation strategy for colloid management and efficient infrared photovoltaics. *Adv. Mater.* **31**, 1805580 (2019).
11. Liu, M. et al. Hybrid organic-inorganic inks flatten the energy landscape in colloidal quantum dot solids. *Nat. Mater.* **16**, 258–263 (2017).
12. Xu, J. et al. 2D matrix engineering for homogeneous quantum dot coupling in photovoltaic solids. *Nat. Nanotechnol.* **13**, 456–462 (2018).
13. Chen, D. et al. Passivating {100} facets of PbS colloidal quantum dots via perovskite bridges for sensitive and stable infrared photodiodes. *Adv. Funct. Mater.* **33**, 2210158 (2023).
14. Vafaie, M. et al. Colloidal quantum dot photodetectors with 10-ns response time and 80% quantum efficiency at 1550 nm. *Matter* **4**, 1042–1053 (2021).
15. Zhang, Y. et al. Electron-transport layers employing strongly bound ligands enhance stability in colloidal quantum dot infrared photodetectors. *Adv. Mater.* **34**, 2206884 (2022).
16. Liu, J. et al. A near-infrared colloidal quantum dot imager with monolithically integrated readout circuitry. *Nat. Electron.* **5**, 443–451 (2022).
17. Gong, X. et al. Highly efficient quantum dot near-infrared light-emitting diodes. *Nat. Photon.* **10**, 253–257 (2016).

18. Goossens, S., Konstantatos, G. & Oikonomou, A. Colloidal quantum dot image sensors: technology and marketplace opportunities. *Inf. Disp.* **37**, 18–23 (2021).
19. Hu, C. et al. Short-wave infrared colloidal quantum dot photodetectors on silicon. *Proc. SPIE* **8631**, 863127 (2013).
20. Guo, J. et al. A photochemical route towards metal sulfide nanosheets from layered metal thiolate complexes. *Angew. Chem.* **131**, 8531–8535 (2019).
21. Cao, Y. et al. Thiolate-mediated photoinduced synthesis of ultrafine $Ag_2S$ quantum dots from silver nanoparticles. *Angew. Chem. Int. Ed.* **55**, 14952–14957 (2016).
22. Shestha, A. et al. Versatile PbS quantum dot ligand exchange systems in the presence of Pb-thiolates. *Small* **13**, 1602956 (2017).
23. Biswas, A. et al. Solution-phase ligand engineering for all-quantum-dot near-infrared light-emitting diodes. *ACS Appl. Nano Mater.* **7**, 9126–9135 (2024).
24. Gilmore, R. H. et al. Epitaxial dimers and auger-assisted detrapping in PbS quantum dot solids. *Matter* **1**, 250–265 (2019).
25. Wang, Y. et al. Silver telluride colloidal quantum dot infrared photodetectors and image sensors. *Nat. Photon.* **18**, 236–242 (2024).
26. Pecunia, V. et al. Assessing the impact of defects on lead-free perovskite-inspired photovoltaics via photoinduced current transient spectroscopy. *Adv. Energy Mater.* **11**, 2003968 (2021).
27. Ollearo, R. et al. Ultralow dark current in near-infrared perovskite photodiodes by reducing charge injection and interfacial charge generation. *Nat. Commun.* **12**, 7277 (2021).
28. Biondi, M. et al. Facet-oriented coupling enables fast and sensitive colloidal quantum dot photodetectors. *Adv. Mater.* **33**, 2101056 (2021).
29. Bi, Y. et al. Infrared solution-processed quantum dot solar cells reaching external quantum efficiency of 80% at 1.35 μm and Jsc in excess of 34 mA cm−2. *Adv. Mater.* **30**, 1704928 (2018).
30. Kemp, K. W. et al. Interface recombination in depleted heterojunction photovoltaics based on colloidal quantum dots. *Adv. Energy Mater.* **3**, 917–922 (2013).
31. Guo, Z., Jena, A. K., Kim, G. M. & Miyasaka, T. The high open-circuit voltage of perovskite solar cells: a review. *Energy Environ. Sci.* **15**, 3171–3222 (2022).
32. Chuang, C. H. M. et al. Open-circuit voltage deficit, radiative sub-bandgap states, and prospects in quantum dot solar cells. *Nano Lett.* **15**, 3286–3294 (2015).
33. Voznyy, O. et al. Origins of stokes shift in PbS nanocrystals. *Nano Lett.* **17**, 7191–7195 (2017).
34. Liu, Y., Kim, D., Morris, O. P., Zhitomirsky, D. & Grossman, J. C. Origins of the stokes shift in PbS quantum dots: impact of polydispersity, ligands, and defects. *ACS Nano* **12**, 2838–2845 (2018).
35. Baumgardner, W. J., Whitham, K. & Hanrath, T. Confined-but-connected quantum solids via controlled ligand displacement. *Nano Lett.* **13**, 3225–3231 (2013).
36. Geuchies, J. J. et al. In situ study of the formation mechanism of two-dimensional superlattices from PbSe nanocrystals. *Nat. Mater.* **15**, 1248–1254 (2016).
37. Keitel, R. C., Weidman, M. C. & Tisdale, W. A. Near-infrared photoluminescence and thermal stability of PbS nanocrystals at elevated temperatures. *J. Phys. Chem.* **120**, 20341–20349 (2016).
38. Choi, H., Ko, J. H., Kim, Y. H. & Jeong, S. Steric-hindrance-driven shape transition in PbS quantum dots: Understanding size-dependent stability. *J. Am. Chem. Soc* **135**, 5278–5281 (2013).
39. Zhao, X. et al. Operationally stable perovskite solar modules enabled by vapor-phase fluoride treatment. *Science* **385**, 433–438 (2024).
40. Luo, J. et al. Polymer-acid-metal quasi-ohmic contact for stable perovskite solar cells beyond a 20,000-hour extrapolated lifetime. *Nat. Commun.* **15**, 2002 (2024).
41. Jiang, Q. et al. Towards linking lab and field lifetimes of perovskite solar cells. *Nature* **623**, 313–318 (2023).
42. Wang, H. et al. PbS Quantum dots ink with months-long shelf-life-time enabling scalable and efficient short-wavelength infrared photodetectors. *Adv. Mater.* **36**, 2311526 (2024).
43. Yin, B. et al. Sensitive organic photodetectors with spectral response up to 1.3 μm using a quinoidal molecular semiconductor. *Adv. Mater.* **36**, 2310811 (2024).
44. Tsai, K. W. et al. Suppressing the dark current while improving the quantum efficiency in shortwave infrared organic photodetectors through naphthalenediimide-based interlayer. *Adv. Opt. Mater* **12**, 2302435 (2024).
45. Zhang, Y. et al. Sensitive SWIR organic photodetectors with spectral response reaching 1.5 μm. *Adv. Mater.* **36**, 2406950 (2024).
46. Pradhan, S., Stavrinadis, A., Gupta, S., Christodoulou, S. & Konstantatos, G. Breaking the open-circuit voltage deficit floor in PbS quantum dot solar cells through synergistic ligand and architecture engineering. *ACS Energy Lett.* **2**, 1444–1449 (2017).
47. Yu, M. et al. In-synthesis Se-stabilization enables defect and doping engineering of HgTe colloidal quantum dots. *Adv. Mater.* **36**, 2311830 (2024).


## Author contributions

G.K. supervised and directed the study. D.M and G.K. conceived the idea, designed this study and co-wrote the manuscript, with feedback from the co-authors. D.M. synthesized the materials, performed the material characterization, fabricated and characterized the devices and analyzed the data. Y.W. contributed to the bandwidth, LDR and photo-induced transient measurements and analysis. C.R. contributed to the TAS measurements and analysis. M.D. measured the cross-sectional SEM image. Ga.K. contributed to temperature dependant J-V measurements. L.P. contributed to TEM and XPS analysis.

## Funding

G.K. acknowledges financial support from the European Research Council (ERC) under the European Union's Horizon 2020 research and innovation program (grant agreement no. 101002306), the Fundació Privada Cellex, the program CERCA and the 'Severo Ochoa' Center of Excellence CEX2019-000910-S funded by the Spanish State Research Agency. C.R. acknowledges MCIU (Ministerio de Ciencia Innovacion y Universidades)/AEI(Agencia Estatal de Investigacion)/10.13039/501100011033 and European Union "NextGenerationEU"/PRTR under the Juan de La Cierva fellowship JDC2022-049722-I.

## Competing interests

G.K and D.M. have filed a patent application. G.K. serves as co-founder, shareholder and scientific advisor at Qurv. The remaining authors declare no competing interests.

## Additional information

**Supplementary information** The online version contains supplementary material available at https://doi.org/10.1038/s41467-026-78740-1.

**Correspondence** and requests for materials should be addressed to Gerasimos Konstantatos.

**Peer review information** *Nature Communications* thanks Kun Ba and other anonymous reviewers for their contribution to the peer review of this work. A peer review file is available.

**Reprints and permissions information** is available at http://www.nature.com/reprints

**Publisher's note** Springer Nature remains neutral with regard to jurisdictional claims in published maps and institutional affiliations.

**Open Access** This article is licensed under a Creative Commons Attribution 4.0 International License, which permits use, sharing, adaptation, distribution and reproduction in any medium or format, as long as you give appropriate credit to the original author(s) and the source, provide a link to the Creative Commons licence, and indicate if changes were made. The images or other third party material in this article are included in the article's Creative Commons licence, unless indicated otherwise in a credit line to the material. If material is not included in the article's Creative Commons licence and your intended use is not permitted by statutory regulation or exceeds the permitted use, you will need to obtain permission directly from the copyright holder. To view a copy of this licence, visit http://creativecommons.org/licenses/by/4.0/.

© The Author(s) 2026

This Article in Press is shared early to give you faster access to new research. It is citable and carries a permanent DOI. The final edited version will replace it automatically.